





**Magnetic phase recognition of artificial kagome spin ice through initial magnetization curve**

Breno Malvezzi Cecchi \*, Nathan Cruz , Marcelo Knobel , and Kleber Roberto Pirota   
*Gleb Wataghin Institute of Physics, State University of Campinas, 13083-859 Campinas, São Paulo, Brazil*



(Received 18 November 2022; revised 20 June 2023; accepted 21 June 2023; published 5 July 2023)

Artificial spin ices (ASIs) are designable arrays of interacting nanomagnets that span a wide range of magnetic phases. Here, we demonstrate that the phase of an artificial kagome spin ice can be identified through its initial magnetization curve. As a proof of concept, micromagnetic simulations of these curves were performed starting from representative microstates of different phases of the system. We show that the curves are characterized by phase-specific features in such a way that a supervised classification algorithm predicts the phase of the initial microstate with good reliability. Moreover, most curves associated with paramagnetic and spin ice 1 phases are recognizable simply by visual inspection. This achievement represents a different strategy for identifying phases in ASIs that is easier and more accessible than magnetic imaging techniques normally used for this task.

DOI: [10.1103/PhysRevB.108.014404](https://doi.org/10.1103/PhysRevB.108.014404)

**I. INTRODUCTION**

Artificial spin ices (ASIs) have proliferated over the past 15 years [1–3]. They are collections of interacting monodomain nanomagnets arranged in designable lattices defined by lithography. In turn, their behavior can be related to several spin lattice models [2]. The ability to directly probe their microstates and to tune their geometry and interactions has made it possible to study the associated statistical mechanics in an unprecedented way. As a result, a wide range of phases have been theoretically predicted and experimentally observed. For example, ASIs can exhibit not only standard ferromagnetic [4–6] and antiferromagnetic [5–7] phases but also more exotic long-range orderings related to the particular lattice geometry [8–14]. Even more interesting are the nontrivial, correlated disordered states they can host due to frustration, such as the ones characteristic of icelike models [15–20], spin liquids [11,18,21,22], spin glasses [23,24], Coulomb phases [18,21,25,26], and string phases [27].

The experimental investigation of the phase diagrams of ASIs is mostly done through magnetic imaging techniques, such as magnetic force microscopy and x-ray photoemission electron microscopy [1–3]. They enable the visualization of each magnetic moment's orientation in real space and possibly in real time. This allows one to know the precise microstates that the system accessed, which is normally impossible when working with bulk materials. In theory, one has all the knowledge required to characterize the occurring phases, phase transitions, and kinetics with this information. For example, a common experiment involves first demagnetizing the sample through a magnetic field protocol to bring the array of nanomagnets to a certain frozen configuration. Then, taking the sample to the proper microscope, it is possible to identify the phase and even the effective temperature of the system by comparing properties extractable from images, such as magnetic moment correlations and vertex populations, with predictions of spin models [11,28–30].

However, there are some practical drawbacks to this image-based strategy. Good high-contrast images can take hours or even days to acquire, taking into account procedures like sample preparation, microscopy calibration, and image processing. Additionally, some experiments can be carried out only in a small number of particular locations, such as synchrotron light sources. Given this, it makes sense to have quicker and easier ways to ascertain the thermodynamic characteristics of ASIs.

The purpose of this work is to propose a strategy to identify the phase of an ASI through its initial magnetization curve, which can be readily measured by several standard magnetometry techniques. Despite their versatility and easy handling, magnetization curves have not been used for this task. The main reason is that the measured magnetization is a property of the whole sample, making it extremely difficult to infer any microstate.

In the following, we focus on an artificial kagome spin ice (AKSI), made up of nanomagnets arranged on a kagome lattice. This is a good ASI prototype to study because the corresponding spin model is known to have a particularly rich phase diagram with four phases [31–33]. At high temperatures, the system is in a paramagnetic (PM) phase, characterized by an uncorrelated disorder. By lowering the temperature, it smoothly accesses a spin liquid phase referred to as spin ice 1 (SI1). In this regime, the system is still disordered at large length scales but locally obeys the kagome ice rules, meaning each vertex has a two-in/one-out or one-in/two-out spin configuration. As the system cools down, it undergoes a phase transition into the intriguing spin ice 2 (SI2) phase, a new spin liquid phase with a number of fascinating properties. Quite interestingly, here, the spins fluctuate only through collective loop moves, preserving the ice rules but also giving rise to long-range ordering of magnetic charges. At a still lower temperature, the system experiences another phase transition and reaches its sixfold degenerate ground state with long-range order (LRO) of both spins and charges.

Our primary hypothesis is that the initial magnetization curve of AKSI retains characteristics related to its starting

\*Corresponding author: [bmcecechi@ifi.unicamp.br](mailto:bmcecechi@ifi.unicamp.br)

point in such a way that the phase of the initial microstate can be deduced solely from the curve. If one applies a magnetic field to drive AKSI from a given microstate to saturation, the exact way the system evolves depends on the initial microstate. On the other hand, microstates of the same phase obey characteristic constraints, as described in the last paragraph. Thus, it is reasonable to expect that evolutions initiating at microstates of the same phase have a greater resemblance to one another than evolutions initiating at microstates of different phases. In turn, the magnetization curves of these processes should also present phase-specific features.

In this work, we provide a proof of concept for this hypothesis. Several microstates were randomly generated for each AKSI phase through Monte Carlo simulations (Sec. II A), and the initial magnetization curves starting from such states were numerically calculated via micromagnetic simulations (Sec. II B). We show that most PM and SI1 curves can be readily recognized from the graphs, but distinguishing between the low-energy, charge-ordered phases is more challenging (Sec. III A). To address this issue, six parameters were defined and calculated for each curve (Sec. III B), allowing us to visualize phase signatures in the curves more precisely from the distribution of the parameters (Sec. III C). Using the parameters as curve features, a supervised classification algorithm is able to recognize the associated phase of the curves with significant accuracy (Sec. III D). A brief physical discussion of the parameters is presented in Sec. III E. This accomplishment paves the way for novel methods of phase recognition in ASIs, and we anticipate that it will spur additional experimental work.

## II. SIMULATIONS

### A. Monte Carlo simulations

A proper description of the effective thermodynamics of an AKSI must take into account the dipolar interaction between the nanomagnets [2,28,34]. Thus, we consider the dipolar Hamiltonian

$$H = - \sum_{i \neq j} J_{ij} S_i S_j, \quad (1)$$

with

$$J_{ij} = - \frac{\mu_0 m^2}{4\pi} \frac{\hat{\mathbf{e}}_i \cdot \hat{\mathbf{e}}_j - 3(\hat{\mathbf{e}}_i \cdot \hat{\mathbf{r}}_{ij})(\hat{\mathbf{e}}_j \cdot \hat{\mathbf{r}}_{ij})}{r_{ij}^3}, \quad (2)$$

where  $m\mathbf{S}_k$  is a magnetic dipole of magnitude  $m$ , located at  $\mathbf{r}_k$ , associated with an Ising spin  $\mathbf{S}_k = S_k \hat{\mathbf{e}}_k$  allowed to point only along direction  $\hat{\mathbf{e}}_k$  with  $S_k = \pm 1$ . A pair of spins  $S_i$  and  $S_j$ , separated by  $\mathbf{r}_{ij} = \mathbf{r}_j - \mathbf{r}_i$ , has the corresponding dipolar coupling strength  $J_{ij}$ .

From this dipolar model, we sampled 20 distinct microstates for five temperatures of each of the four phases of the system. This amounts to four sets of 100 microstates, with each set representing a given phase. The microstates were randomly generated by performing Monte Carlo simulations of a  $12 \times 12$  kagome lattice with periodic boundary conditions. We employed the Metropolis algorithm with both single spin flip and spin loop flip dynamics and used 200 Monte Carlo steps per spin (MCS/spin) for thermalization. The temperatures were chosen to be well spaced but

also as distant as possible from the transition temperatures. The latter were estimated through the peaks of the specific heat (shown in the Supplemental Material [35]) and were found to be  $k_B T / |J_1| \sim 2.0$  for PM/SI1,  $\sim 0.17$  for SI1/SI2, and  $\sim 0.089$  for SI2/LRO, where  $J_1$  is the nearest-neighbor coupling strength.

We emphasize that the sets of microstates associated with the PM, SI1, and SI2 phases are representative samples of these extensively degenerate phases.<sup>1</sup> Indeed, the spin correlations of the selected microstates distribute well around the thermodynamic mean values of the dipolar model, as shown in Fig. 1. The latter were calculated from independent Monte Carlo simulations for a greater number of temperatures using  $\sim 10^3$  to  $\sim 10^4$  MCS/spin for measurements, which averaged between 300 and 3000 microstates depending on temperature.

On the other hand, the long-range ordered ground state is only sixfold degenerate. However, our supervised classification algorithm needs a training set with more than just six data sets to be able to identify a given phase, making it impossible to include the true LRO phase in our statistical analysis. To circumvent this issue, we exploited the fact that our simulated kagome lattice is still able to fluctuate for temperatures not very much below its SI2/LRO transition temperature. Thus, for each of the five chosen LRO temperatures, we waited long enough for the system to access 20 new distinct configurations. As a result, we collected 100 distinct microstates that are actually a mixture of LRO and SI2 phases but have considerable predominance of LRO. Namely, at least 85% of the spins obey the LRO pattern, and the remaining part respects only SI2 constraints [35]. Because of this, we will refer to this phase as ‘‘quasi-long-range order’’ (QLRO). Correspondingly, the QLRO spin correlations are centered slightly off the characteristic LRO values but are still markedly different from those of the other phases, as can be seen in Fig. 1.

### B. Micromagnetic simulations

The whole set of 400 distinct microstates was used as the initial states in micromagnetic simulations of an analogous  $12 \times 12$  kagome lattice of nanomagnets. In order to do that, we set the magnetization of each nanomagnet to be uniform with the same orientation of the corresponding spin of the microstate, as illustrated in Fig. 2, and then the system was relaxed. For each initial state, the initial magnetization curve was calculated by applying the field in the  $y$  direction (see Fig. 2). In addition, we considered stadium-shaped nanomagnets with a length of 300 nm, width of 100 nm, and thickness of 20 nm. Open boundary conditions were used because that is the case in a real sample. The simulations were performed with MUMAX3 [35,36], using edge smoothing,<sup>2</sup> cells with dimensions of  $4.4 \times 4.2 \times 20$  nm<sup>3</sup>, and material parameters of permalloy: saturation magnetization  $M_s = 8 \times 10^5$  A/m and exchange stiffness  $A_{\text{ex}} = 1 \times 10^{-11}$  J/m.

<sup>1</sup>They were sampled at each 10 MCS/spin, which is longer than the autocorrelation time of the system.

<sup>2</sup>Simulations without edge smoothing provided similar results, with the initial magnetization curves approximately shifted rigidly to the right.

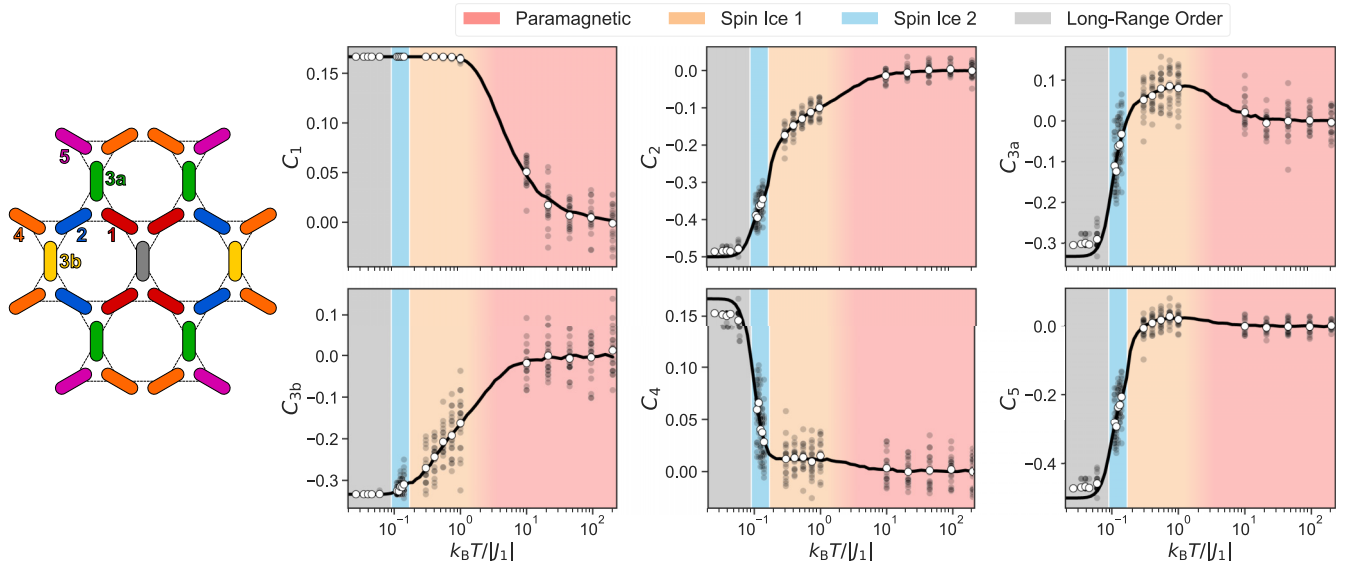


FIG. 1. Spin correlations  $C_n = \langle \mathbf{S}_i \cdot \mathbf{S}_j \rangle_n$  between  $n$ th neighbors of kagome spin ice for  $n = 1, 2, 3a, 3b, 4, 5$  (as indicated in the left panel) as a function of temperature  $T$ . Gray dots are the values for each sampled microstate, white dots are the averages over the 20 microstates sampled at the same temperature, and solid black lines are the thermodynamic means of the dipolar model.

### III. PHASE RECOGNITION THROUGH THE INITIAL MAGNETIZATION CURVE

#### A. Initial magnetization curves

Figure 3 shows the averages over the 100 initial magnetization curves of each phase, which gives a general view of how different the curves are based on their associated phase. For  $25 \lesssim \mu_0 H \lesssim 50$  mT, the curves differ from one another for more than one standard deviation, except between SI2 and QLRO. Thus, it is safe to say that one can distinguish between PM, SI1, and SI2 combined with QLRO directly by looking at the graphs.

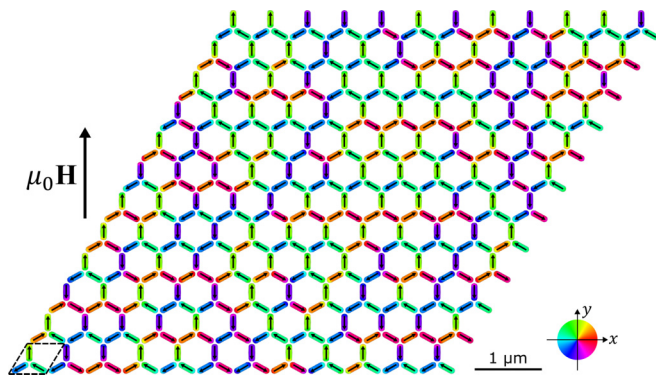


FIG. 2. One of the initial states of micromagnetic simulations of a  $12 \times 12$  kagome lattice (a unit cell is highlighted in the bottom left). The arrows indicate the spins of a microstate representative of the SI1 phase, taken from Monte Carlo simulations. To set the initial state, a uniform magnetization was assigned to each nanomagnet following the same orientation of the corresponding spin, and the system was relaxed. The initial magnetization curve was simulated by applying a magnetic field  $\mu_0 \mathbf{H}$  in the  $y$  direction. The color code represents the local direction of the magnetization.

Distinguishing SI2 from QLRO curves by eye is much more challenging because they have considerable overlap. This makes intuitive sense because the microstates of these phases are more similar to one another because they share more characteristic constraints (namely, ice rules and charge ordering). Besides that, it is desirable to have a way to recognize each phase that is less subjective than visual inspection.

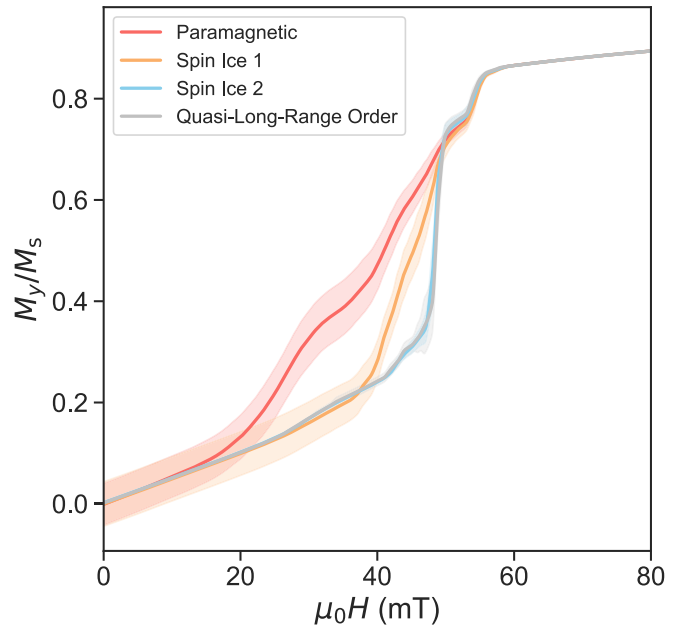


FIG. 3. Average initial magnetization curves of each AKSI phase, calculated from the 100 curves associated with each phase. Uncertainty represents one standard deviation.

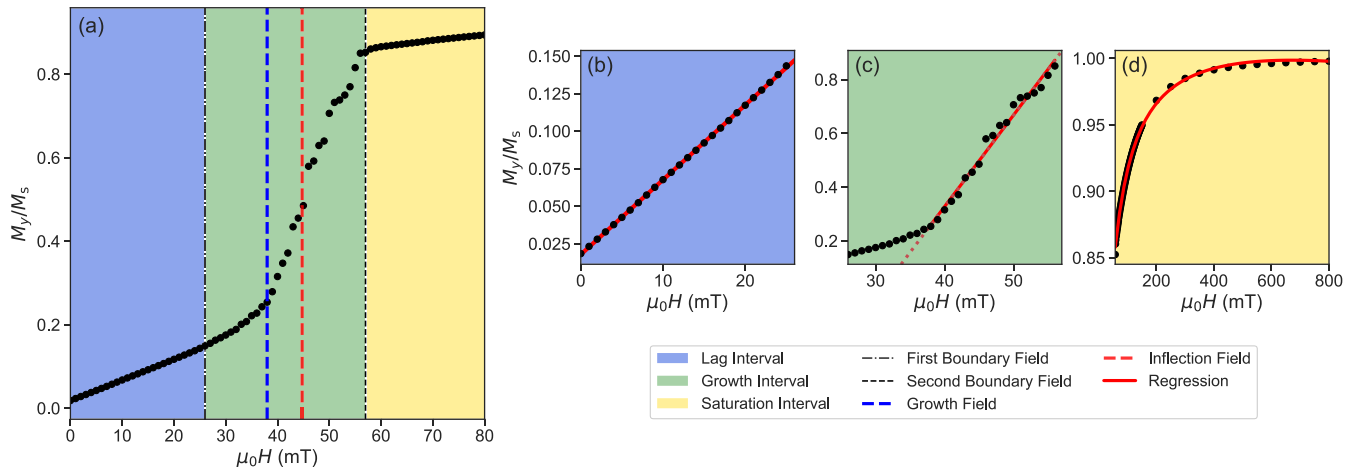


FIG. 4. (a) One of the initial magnetization curves starting from a SI2 microstate. It shows the three intervals separated by the boundary fields  $\mu_0 H_{b1}$  and  $\mu_0 H_{b2}$ . (b) Lag interval, where we perform a linear fit to extract the initial magnetic susceptibility  $\chi_i$  as the angular coefficient. (c) Growth interval, where we calculate the growth length  $s_g$ , the growth field  $\mu_0 H_g$ , the inflection field  $\mu_0 H_{flex}$ , and the growth slope  $\alpha_g$  of the linear fit performed in the magnetization's steep rise region. (d) Saturation interval, where magnetization is well fitted by the law of approach to saturation.

### B. Curve parameters

To address these issues, we defined common parameters for all curves. Each curve was divided into three regions separated by the first and second boundary fields  $\mu_0 H_{b1}$  and  $\mu_0 H_{b2}$ , respectively, as shown in Fig. 4(a). We call the lag interval [Fig. 4(b)] the first part of the magnetization curve for  $H \leq H_{b1}$ , where the behavior is essentially linear. In this region, the curve is well fitted by a straight line whose angular coefficient can be identified as the initial magnetic susceptibility  $\chi_i$ .

The growth interval [Fig. 4(c)], corresponding to  $H_{b1} \leq H \leq H_{b2}$ , begins at  $H = H_{b1}$ , where the curve starts to deviate from its initial linear trend, and ends at  $H = H_{b2}$ , where the sample starts to approach saturation. In this interval, the curve's behavior is more complex, containing most of its particular features. Here, we considered the following four parameters: (i) the growth length  $s_g$ , defined as the arc length of the curve; (ii) the inflection field  $\mu_0 H_{flex}$ , defined as the lowest field of an inflection point; (iii) the growth field  $\mu_0 H_g$ , taken to be the field at which a steeper increase of magnetization occurs; and (iv) the growth slope  $\alpha_g$ , which represents the average slope of the curve in the subinterval of steeper increase of magnetization and is calculated as the angular coefficient of the linear regression shown in Fig. 4(c). A detailed explanation of how all parameters were computed is given in the Supplemental Material [35].

Finally, in the saturation interval [Fig. 4(d)], where  $H \geq H_{b2}$ , the magnetization follows the well-known law of approach to saturation [37]. However, this interval does not carry any information about the initial configuration since the magnetic moments of all nanomagnets are already nearly aligned with the field and all curves practically coincide.

### C. Parameter distribution

The following six parameters have proved useful in identifying the AKSI phases:  $\mu_0 H_{b1}$ ,  $\chi_i$ ,  $s_g$ ,  $\mu_0 H_{flex}$ ,  $\mu_0 H_g$ , and

$\alpha_g$ . Figure 5 displays the distribution of these parameters for each phase. Note how the PM and SI1 distributions of most parameters are well separated from one another and from those of SI2 and QLRO. This is particularly clear in the  $\mu_0 H_g$  distribution [Fig. 5(d)]. However, for all cases, the SI2 and QLRO distributions are centered at very close values and have considerable overlap.

Another way to visualize the parameter distribution comes from applying a principal component analysis (PCA) to our data. In this method, the parameters describe a six-dimensional space, where each of our curves is represented by a point. In this space, the vector for which the variance of the projected points is maximized is called the first principal component; its orthonormal vector that maximizes the variance is called the second principal component. The two-dimensional subspace spanned by the first and second principal components, shown in Fig. 6, is the plane that better represents the data distribution. This dimensionality reduction retains meaningful features of the original data and allows one to visualize clusters of points with common properties. Indeed, one sees again that the sets of points for PM, SI1, and SI2 combined with QLRO are well separated, whereas the individual SI2 and QLRO sets overlap. It is also worth noting that the greater the phase degeneracy is, the wider its distribution of parameters is, and consequently, the larger its cluster is.

### D. Supervised classification algorithm

The distributions shown in Figs. 5 and 6 suggest that it is possible to identify the associated phase of each curve, with the exception of distinguishing between SI2 and QLRO. To really verify this, the parameters of  $\sim 70\%$  of the curves were used as a training data set for a supervised classification algorithm, the so-called support vector machine [35,38], to classify the remaining  $\sim 30\%$  of the test curves.

The performance of the classifier is summarized in Table I. As expected, the algorithm correctly predicted the phase of all 34 PM and 38 SI1 test curves. In addition, it correctly



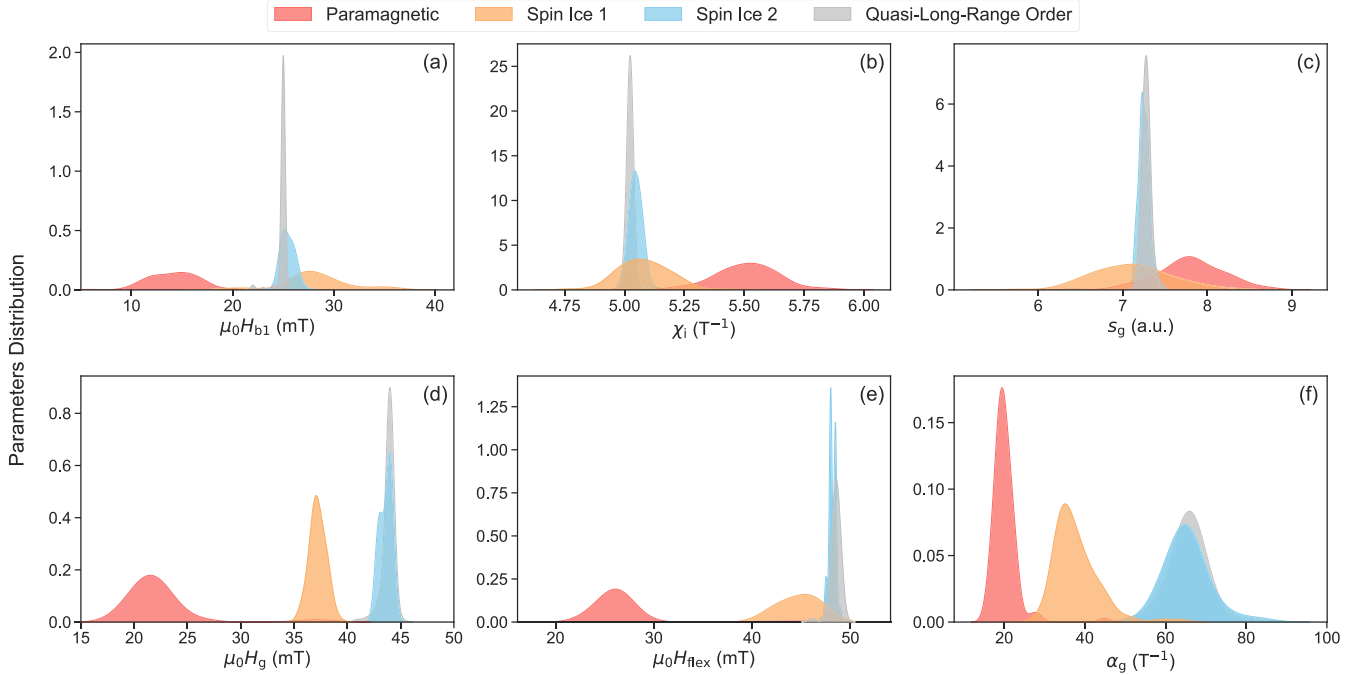


FIG. 5. Normalized distributions for each phase of the (a) first boundary field  $\mu_0 H_{b1}$ , (b) initial magnetic susceptibility  $\chi_i$ , (c) growth length  $s_g$ , (d) growth field  $\mu_0 H_g$ , (e) inflection field  $\mu_0 H_{flex}$ , and (f) growth slope  $\alpha_g$ .

determined the phase of 24 out of the 27 SI2 test curves, whereas the other 3 were misclassified as QLRO; it correctly determined the phase of 25 out of the 33 QLRO curves, whereas the other 8 were misclassified as SI2. This distinction between SI2 and QLRO is astonishingly good: considering the apparent equivalence between the curves of those phases, a mistake percentage of only  $\sim 20\%$  is impressive. Moreover,

some of the errors may be related to the mix of LRO and SI2 in the QLRO microstates.

### E. Physical discussion

Finally, we address some of the physics underlying our six parameters. Figure 7 shows how they change as a function of the effective temperature. Even when the change is not monotonic, one sees that, as the temperature increases,  $\chi_i$  increases [Fig. 7(a)] and  $\mu_0 H_{b1}$ ,  $\mu_0 H_{flex}$ , and  $\mu_0 H_g$  decrease [Figs. 7(b), 7(f), and 7(d), respectively]. All these general trends indicate that the magnetic behavior of the AKSI gets softer with increasing effective temperature. We also observe that  $\mu_0 H_{b2}$  remains practically constant (see the Supplemental Material [35]), which is reasonable since the saturation field should be the same for demagnetized initial states. As a consequence of the magnetic softening with effective temperature and of the constancy of  $\mu_0 H_{b2}$ ,  $\alpha_g$  decreases, and  $s_g$  increases with temperature, as can be seen in Figs. 7(e) and 7(c).

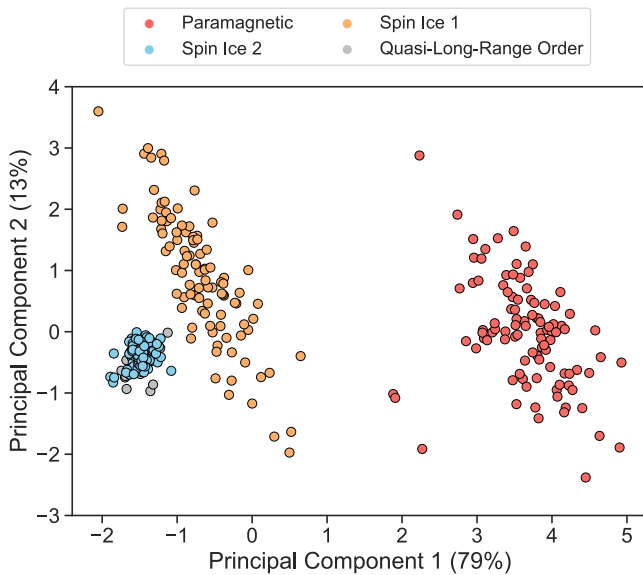


FIG. 6. PCA scatterplot of the points representing the six parameters of each initial magnetization curve. The data variances with respect to the first and second principal components are, respectively, 75% and 13% of the total variance.

TABLE I. Performance metrics of the support vector machine classifier for identifying the AKSI phase from parameters of initial magnetization curves. Accuracy is 0.92.

	Precision	Recall	F <sub>1</sub> score
Paramagnetic	1.00	1.00	1.00
Spin ice 1	1.00	1.00	1.00
Spin ice 2	0.75	0.89	0.81
Quasi-long-range order	0.89	0.76	0.82

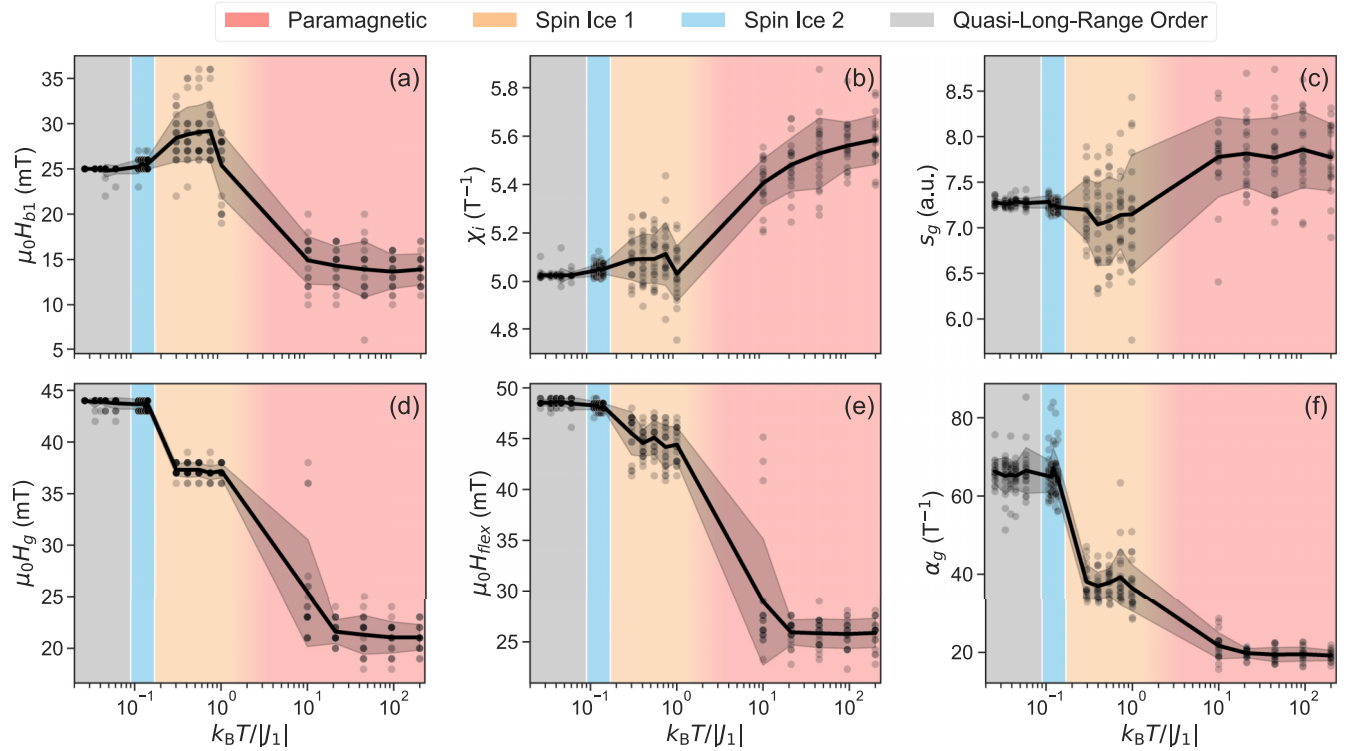


FIG. 7. Dependence on effective temperature  $T$  of the (a) first boundary field  $\mu_0 H_{b1}$ , (b) initial magnetic susceptibility  $\chi_i$ , (c) growth length  $s_g$ , (d) growth field  $H_g$ , (e) inflection field  $\mu_0 H_{flex}$ , and (f) angular coefficient  $\alpha_g$ . Gray dots are the parameter values for each sampled microstate, black curves are the averages over all microstates sampled at the same temperature, and uncertainties represent one standard deviation.

#### IV. CONCLUSION AND PERSPECTIVES

This study's key finding is that the AKSI's initial magnetization curve preserves a significant amount of information on the phase of its original microstate. We showed that such curves may be utilized to assist with the identification of the phases using a supervised classification algorithm. Even so, more research with larger samples is needed to assess how the separation between the SI2 and QLRO phases improves when the SI2 proportion in the mixed SI2/LRO microstates decreases. Also, in order to better understand the parameter distributions and see how they react at the critical points, it would be intriguing to include temperatures closer to the phase transitions.

Furthermore, it would be rather simple to apply similar research to different ASI geometries. By examining the patterns shared by a certain collection of magnetization curves, which might be challenging to recognize by eye, one may be able to decode the physics inherent in a particular ASI magnetization process. On the other hand, imperfections inevitably present in experimental samples, such as roughness and grains, are known to affect the magnetization curve [39,40], so their impact on the recognition process should also be addressed.

Our findings thus open the door to the experimental determination of ASI magnetic phases using only magnetometry techniques, which are more widely utilized and user-friendly than the magnetic imaging methods often employed for this type of study. Moreover, the phase recognition could be carried out right after a field-driven demagnetization protocol,

using the same magnetometer. However, this does not mean that the proposed strategy completely replaces imaging experiments because certain insights into the physics of ASIs may be gained only by knowing the precise microstate—and not only its phase. Rather, the best investigation approach is probably a combination of both tools. For example, one may wish to measure the magnetization curve to quickly verify whether the sample is in the desired phase before probing it with complementary images. We are confident that, once improved, this will grow into a potent analysis method for studying complex magnetic phases, possibly expanding future experimental studies.

As a final remark, we note that a very interesting extension of this work would be the development of unsupervised classification algorithms instead of supervised ones. This would be especially useful for investigating new ASIs for which the phase diagram is still unknown. The algorithm would be able to separate measured magnetization curves into groups that are not predefined and thereby identify distinct phases.

#### ACKNOWLEDGMENTS

The authors acknowledge D. Navas for help with writing the micromagnetic simulation codes, São Paulo Research Foundation for financial support through Grants No. 2017/10581-1, No. 2019/23317-6, and No. 2023/00137-8, and INCT of Spintronics and Advanced Magnetic Nanostructures (INCT-Spin-NanoMag) for financial support through CNPq Grant No. 406836/2022-1.

- [1] C. Nisoli, R. Moessner, and P. Schiffer, *Rev. Mod. Phys.* **85**, 1473 (2013).
- [2] N. Rougemaille and B. Canals, *Eur. Phys. J. B* **92**, 62 (2019).
- [3] S. H. Skjærvø, C. H. Marrows, R. L. Stamps, and L. J. Heyderman, *Nat. Rev. Phys.* **2**, 13 (2020).
- [4] Y. Li, G. W. Paterson, G. M. Macauley, F. S. Nascimento, C. Ferguson, S. A. Morley, M. C. Rosamond, E. H. Linfield, D. A. MacLaren, R. Macêdo, C. H. Marrows, S. McVitie, and R. L. Stamps, *ACS Nano* **13**, 2213 (2019).
- [5] E. Digernes, S. D. Sløetjes, A. Strømberg, A. D. Bang, F. K. Olsen, E. Arenholz, R. V. Chopdekar, J. K. Grepstad, and E. Folven, *Phys. Rev. Res.* **2**, 013222 (2020).
- [6] V. M. Parakkat, G. M. Macauley, R. L. Stamps, and K. M. Krishnan, *Phys. Rev. Lett.* **126**, 017203 (2021).
- [7] J. P. Morgan, A. Stein, S. Langridge, and C. H. Marrows, *Nat. Phys.* **7**, 75 (2011).
- [8] I. A. Chioar, N. Rougemaille, and B. Canals, *Phys. Rev. B* **93**, 214410 (2016).
- [9] J. Sklenar, Y. Lao, A. Albrecht, J. D. Watts, C. Nisoli, G.-W. Chern, and P. Schiffer, *Nat. Phys.* **15**, 191 (2019).
- [10] J. Lehmann, C. Donnelly, P. M. Derlet, L. J. Heyderman, and M. Fiebig, *Nat. Nanotechnol.* **14**, 141 (2019).
- [11] V. Schánilec, B. Canals, V. Uhlir, L. Flajšman, J. Sadilek, T. Šíkola, and N. Rougemaille, *Phys. Rev. Lett.* **125**, 057203 (2020).
- [12] H. Saglam, A. Duzgun, A. Kargioti, N. Harle, X. Zhang, N. S. Bingham, Y. Lao, I. Gilbert, J. Sklenar, J. D. Watts, J. Ramberger, D. Bromley, R. V. Chopdekar, L. O'Brien, C. Leighton, C. Nisoli, and P. Schiffer, *Nat. Phys.* **18**, 706 (2022).
- [13] K. Hofhuis, S. H. Skjærvø, S. Parchenko, H. Arava, Z. Luo, A. Kleibert, P. M. Derlet, and L. J. Heyderman, *Nat. Phys.* **18**, 699 (2022).
- [14] W.-C. Yue, Z. Yuan, Y.-Y. Lyu, S. Dong, J. Zhou, Z.-L. Xiao, L. He, X. Tu, Y. Dong, H. Wang, W. Xu, L. Kang, P. Wu, C. Nisoli, W.-K. Kwok, and Y.-L. Wang, *Phys. Rev. Lett.* **129**, 057202 (2022).
- [15] R. F. Wang, C. Nisoli, R. S. Freitas, J. Li, W. McConville, B. J. Cooley, M. S. Lund, N. Samarth, C. Leighton, V. H. Crespi, and P. Schiffer, *Nature (London)* **439**, 303 (2006).
- [16] M. Tanaka, E. Saitoh, H. Miyajima, T. Yamaoka, and Y. Iye, *Phys. Rev. B* **73**, 052411 (2006).
- [17] Y. Qi, T. Brintlinger, and J. Cumings, *Phys. Rev. B* **77**, 094418 (2008).
- [18] Y. Perrin, B. Canals, and N. Rougemaille, *Nature (London)* **540**, 410 (2016).
- [19] Y. Perrin, B. Canals, and N. Rougemaille, *Phys. Rev. B* **99**, 224434 (2019).
- [20] V. Schánilec, O. Brunn, M. Horáček, S. Krátký, P. Meluzín, T. Šíkola, B. Canals, and N. Rougemaille, *Phys. Rev. Lett.* **129**, 027202 (2022).
- [21] E. Östman, H. Stopfel, I.-A. Chioar, U. B. Arnalds, A. Stein, V. Kapaklis, and B. Hjörvarsson, *Nat. Phys.* **14**, 375 (2018).
- [22] J. Colbois, K. Hofhuis, Z. Luo, X. Wang, A. Hrabec, L. J. Heyderman, and F. Mila, *Phys. Rev. B* **104**, 024418 (2021).
- [23] M. Saccone, A. Scholl, S. Velten, S. Dhuey, K. Hofhuis, C. Wuth, Y.-L. Huang, Z. Chen, R. V. Chopdekar, and A. Farhan, *Phys. Rev. B* **99**, 224403 (2019).
- [24] M. Saccone, F. Caravelli, K. Hofhuis, S. Parchenko, Y. A. Birkhölzer, S. Dhuey, A. Kleibert, S. van Dijken, C. Nisoli, and A. Farhan, *Nat. Phys.* **18**, 517 (2022).
- [25] B. Canals, I.-A. Chioar, V.-D. Nguyen, M. Hehn, D. Lacour, F. Montaigne, A. Locatelli, T. O. Menteş, B. S. Burgos, and N. Rougemaille, *Nat. Commun.* **7**, 11446 (2016).
- [26] A. Farhan, M. Saccone, C. F. Petersen, S. Dhuey, R. V. Chopdekar, Y.-L. Huang, N. Kent, Z. Chen, M. J. Alava, T. Lippert, A. Scholl, and S. van Dijken, *Sci. Adv.* **5**, eaav6380 (2019).
- [27] X. Zhang, A. Duzgun, Y. Lao, S. Subzwari, N. S. Bingham, J. Sklenar, H. Saglam, J. Ramberger, J. T. Batley, J. D. Watts, D. Bromley, R. V. Chopdekar, L. O'Brien, C. Leighton, C. Nisoli, and P. Schiffer, *Nat. Commun.* **12**, 6514 (2021).
- [28] I. A. Chioar, N. Rougemaille, A. Grimm, O. Fruchart, E. Wagner, M. Hehn, D. Lacour, F. Montaigne, and B. Canals, *Phys. Rev. B* **90**, 064411 (2014).
- [29] I. A. Chioar, B. Canals, D. Lacour, M. Hehn, B. Santos Burgos, T. O. Menteş, A. Locatelli, F. Montaigne, and N. Rougemaille, *Phys. Rev. B* **90**, 220407(R) (2014).
- [30] K. Hofhuis, A. Hrabec, H. Arava, N. Leo, Y.-L. Huang, R. V. Chopdekar, S. Parchenko, A. Kleibert, S. Koraltan, C. Abert, C. Vogler, D. Suess, P. M. Derlet, and L. J. Heyderman, *Phys. Rev. B* **102**, 180405(R) (2020).
- [31] G. Möller and R. Moessner, *Phys. Rev. B* **80**, 140409(R) (2009).
- [32] G.-W. Chern, P. Mellado, and O. Tchernyshyov, *Phys. Rev. Lett.* **106**, 207202 (2011).
- [33] G.-W. Chern and O. Tchernyshyov, *Philos. Trans. R. Soc. A* **370**, 5718 (2012).
- [34] N. Rougemaille, F. Montaigne, B. Canals, A. Duluard, D. Lacour, M. Hehn, R. Belkhou, O. Fruchart, S. El Moussaoui, A. Bendounan, and F. Maccherozzi, *Phys. Rev. Lett.* **106**, 057209 (2011).
- [35] See Supplemental Material at <http://link.aps.org/supplemental/10.1103/PhysRevB.108.014404> for further details on estimate of the transition temperatures, LRO faction distribution over QLRO microstates, calculation of initial magnetization curve parameters and effective temperature dependence of second boundary field. We also provide the codes and data related to the micromagnetic and Monte Carlo simulations, curve parameters computation and supervised classifier.
- [36] A. Vansteenkiste, J. Leliaert, M. Dvornik, M. Helsen, F. Garcia-Sanchez, and B. Van Waeyenberge, *AIP Adv.* **4**, 107133 (2014).
- [37] B. D. Cullity and C. D. Graham, *Introduction to Magnetic Materials*, 2nd ed. (Wiley, Hoboken, NJ, 2009), pp. 325–326.
- [38] F. Pedregosa, G. Varoquaux, A. Gramfort, V. Michel, B. Thirion, O. Grisel, M. Blondel, P. Prettenhofer, R. Weiss, V. Dubourg, J. Vanderplas, A. Passos, D. Cournapeau, M. Brucher, M. Perrot, and E. Duchesnay, *J. Mach. Learn. Res.* **12**, 2825 (2011).
- [39] K. K. Kohli, A. L. Balk, J. Li, S. Zhang, I. Gilbert, P. E. Lammert, V. H. Crespi, P. Schiffer, and N. Samarth, *Phys. Rev. B* **84**, 180412(R) (2011).
- [40] M. F. Velo, B. M. Cecchi, and K. R. Pirota, *Phys. Rev. B* **102**, 224420 (2020).